Journal of Membrane Science 700 (2024) 122677

Contents lists available at ScienceDirect

Journal of Membrane Science

journal homepage: www.elsevier.com/locate/memsci

Preparation of ZIF-62 polycrystalline and glass membranes for helium separation

Zhijun Zhao [a,*], Li Ding [b], Alexander Mundstock [a], Oliver Stölting [c], Sebastian Polarz [c], Haihui Wang [b], Armin Feldhoff [a,**]

[a] Leibniz University Hannover, Institute of Physical Chemistry and Electrochemistry, 30167, Hannover, Germany
[b] Tsinghua University, Department of Chemical Engineering, 100084, Beijing, China
[c] Leibniz University Hannover, Institute of Inorganic Chemistry, 30167, Hannover, Germany

ARTICLE INFO

Keywords:
ZIF-62 membrane
MXene
MOF glass
Gas separation
Helium recovery

ABSTRACT

Defects among the grains of MOF polycrystalline membranes lead to non-selective gas transport, thereby reducing their selectivity in gas separation. In this work, ZIF-62 polycrystalline membranes with a well-intergrown structure were prepared on MXene-modified supports. Subsequent thermal treatment transformed the membranes into glass membranes, effectively eliminating non-selective defects at grain boundaries. Due to the incorporation of the MXene film and the vertical positioning of the support during the solvothermal process, only a minimal portion of the glass melt infiltrated into the porous support. Across the temperature range of 303 K–423 K and pressure range of 1 bar–3 bar, the ZIF-62 glass membranes showcased superior helium separation property and long-term chemical stability (resistant to CO_2 and H_2O). The helium permeance reached approximately 51 GPU, with selectivities against N_2 and CH_4 being 17.4 and 13.9, respectively, outperforming current MOF membranes.

1. Introduction

Helium, as a noble gas, exhibits unique properties (e.g. low boiling point, small molecular size, inertness) that make it indispensable in various industries, including its use as a coolant, leak detector, protective gas in welding, and carrier gas in gas chromatography [1]. However, the challenge lies in sourcing helium, as it is primarily found in natural gas fields with concentrations mostly between 0.3% and 1.9% [2,3]. The low concentration, combined with its unique properties of a low boiling point and low polarizability, renders conventional recovery methods, such as cryogenic distillation and pressure swing adsorption, both energy and capital inefficient [4]. In response to these challenges, membrane-based separation has emerged as a promising alternative since it offers low energy consumption, a reduced carbon footprint, and more straightforward operation [5–8]. Polymers were among the first materials investigated for membrane-based helium separation, with the commercialization of polyimide membrane representing a significant milestone [9,10]. However, polymer membranes exhibit a trade-off between permeability and selectivity due to their reliance on the solution-diffusion transport mechanism [8,11]. Introducing inorganic particles into a continuous polymer membrane, the so-called mixed matrix membranes (MMM), can improve the separation of helium [12,13]. Nevertheless, the polymer phase, regardless as pure form or as MMM, is susceptible to challenges like plasticization and swelling [14,15]. A different separation strategy relies on the molecular sieving effect, where the pore size is comparable to the kinetic diameter of helium [16,17]. Through pyrolyzing polymer in a controlled gas atmosphere, carbon molecular sieve (CMS) membranes with tunable pore size and distribution can be formed, where ultramicropores derived from stacking of strands can be tuned to 0.34 nm by increasing the carbonization temperature [18–22]. In addition, silica membranes also hold advantages over polymeric ones due to their small pores and rigid structure [23]. In-depth comparison on various membrane materials for He separation can be found in recent reviews [8,11].

Metal-organic frameworks (MOFs) are garnering substantial attention as emerging membrane materials, although many of those have demonstrated disappointingly low selectivities for He/N_2 and He/CH_4 separations, often below a selectivity of 5 [8,24]. In the pursuit of higher

* Corresponding author.
** Corresponding author.
E-mail addresses: zhijun.zhao@pci.uni-hannover.de (Z. Zhao), armin.feldhoff@pci.uni-hannover.de (A. Feldhoff).

https://doi.org/10.1016/j.memsci.2024.122677
Received 8 January 2024; Received in revised form 15 March 2024; Accepted 18 March 2024
Available online 19 March 2024
0376-7388/© 2024 The Authors. Published by Elsevier B.V. This is an open access article under the CC BY license (http://creativecommons.org/licenses/by/4.0/).

selectivity, Chen et al. [25] showcased a single crystal ZIF-8 membrane without grain boundaries, achieving a remarkable He/CH_4 selectivity up to 40. While single crystal membranes might not be feasible for broader applications, this advancement emphasizes the capabilities of MOF membranes when the inherent challenge, i.e. defects at grain boundaries, can be effectively tackled. However, polycrystalline MOF membranes – integrated by intergrown crystals – suffer in particular from defects at grain boundaries, which serve as preferential pathways for non-selective transport and impair the gas selectivity [26–28]. To enhance the selectivity of polycrystalline membranes comparable to single crystal membranes, approaches have been explored such as low-temperature synthesis [29], careful activation (i.e. removal of solvent molecules from grains) [26,30], defects healing by coating polymer [31,32], and partial amorphization either during synthesis or via post-modification [33–38].

Amid this evolving landscape, MOF glass membranes emerge as another promising avenue garnering significant scientific interest since their porosity can be preserved during the crystal-liquid-glass transformation [39–41], whereas the liquid state enables good processability and elimination of non-selective defects at grain boundaries [42–52]. Initial research on MOF glasses started with amorphous ZIF-4 but soon shifted its lens towards ZIF-62, primarily due to its lower melting point and a broader melting range [53,54]. To the best of our knowledge, most MOF glass membranes are prepared from their respective powders, either by in-situ deposition in a solution or by ex-situ compression in a mold, because ZIF-62 tends to nucleate in solution instead of on support [43–47,55,56]. Wang et al. [43] deposit ZIF-62 powder onto a horizontally placed support and then apply a thermal treatment to produce a ZIF-62 glass membrane. During the liquid-solid transformation, defects (gaps, pinholes, and grain boundaries) are eliminated and the resulting ZIF-62 glass membrane displays high ideal selectivities, with CO_2/N_2 equaling 23, which is close to the selectivity of 29 observed in the single crystal ZIF-8 membrane [25,43]. However, parts of the glass membrane produced by Wang et al. [43] infiltrate heavily into the support, as evidenced by the Zn signal in the elemental distribution analysis of a membrane cross-section. While the infiltration enhances the membrane-support interaction, it may affect the evaluation of the membrane's performance.

In recent studies, the application of a two-dimensional material known as MXene has gained prominence in separation membrane materials [57–59]. These nanosheets exhibit a wealth of surface charges. Leveraging this characteristic, MXene films can be effectively fabricated within an electric field [60]. Furthermore, these nanosheets offer the capability for the in-situ synthesis of MOF crystals and membranes owing to their electrostatic interaction with cations [61,62]. In this work, we report the preparation of ZIF-62 polycrystalline membranes using vertically placed supports with the assistance of Zn (II) adsorbed/intercalated $Ti_3C_2T_x$ MXene films (T stands for surface terminations). These polycrystalline membranes were subsequently vitrified to produce ZIF-62 glass membranes. We anticipate that the vertically oriented support and the stacked layers of MXene nanosheets will limit the infiltration of glass melt into the support, providing better control over the membrane thickness. Due to the elimination of non-selective defects, improved helium selectivity over nitrogen and methane is expected in ZIF-62 glass membranes.

2. Material and methods

All chemicals were purchased from Alfa Aesar and used without further purification unless otherwise stated. The synthesis of ZIF-62 polycrystalline and glass membranes is depicted in Fig. 1. The process involves four key steps: generating MXene nanosheets and filtering them onto a porous Al_2O_3 disk to create a MXene thin film; intercalating/adsorbing Zn (II) ions into the film; solvothermally synthesizing ZIF-62 polycrystalline membrane, which was subsequently transformed into a glass membrane through vitrification.

2.1. Preparation of Zn (II)-MXene films

The Zn (II)-MXene film was prepared following a previously reported method with slight modifications [24]. To produce MXene nanosheets, 1 g Ti_3AlC_2 powder (Laizhou Kai Kai Ceramic Materials Co., Ltd) was slowly added into an etchant composed of LiF and 9 M hydrochloric acid. After stirring at 309 K for 24 h, sediment from the mixture was collected and washed to a neutral pH (>6) using deionized water. In a typical procedure, the sediment was then dispersed in deionized water and ultrasonicated (Bandelin RK 31, 40 Watt) for 60 min, followed by centrifugation (Sigma 3-18KS) at 5200 rpm for 60 min. To prepare a Zn

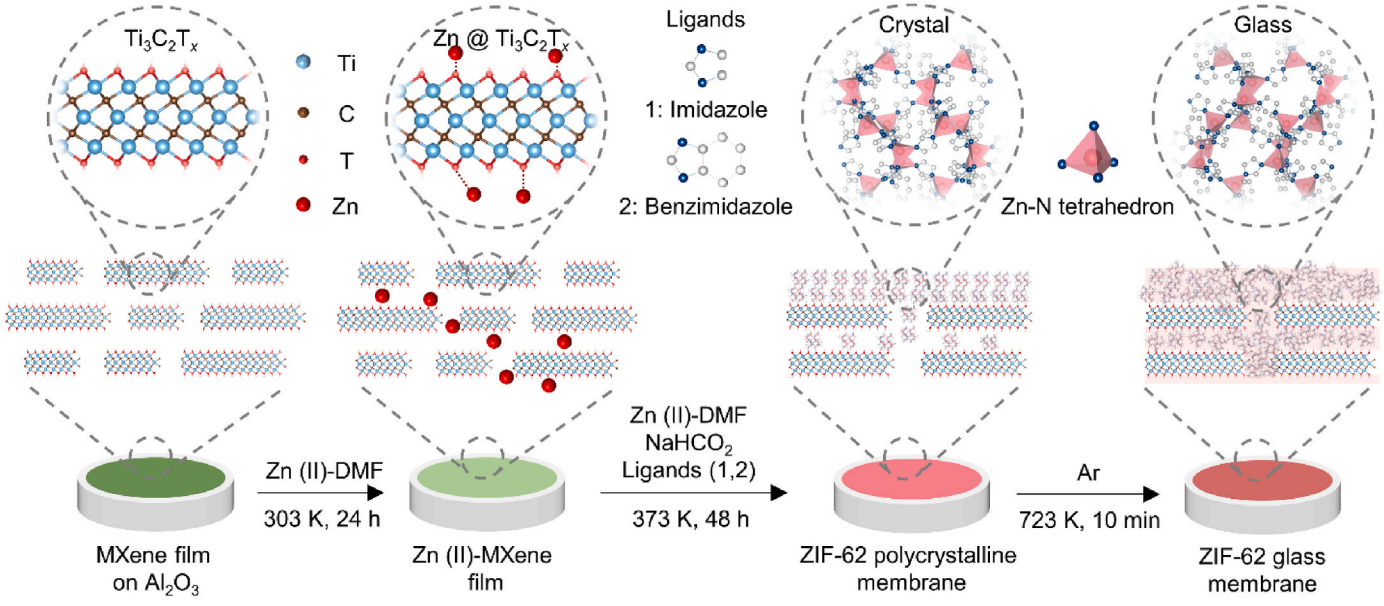

Fig. 1. Schematic representation of the fabrication process for a ZIF-62 glass membrane on a MXene-modified α-Al_2O_3 disk. The termination groups (e.g., –OH, =O, and –F) of MXene nanosheets are denoted as T. Structures of ZIF-62 crystal and glass are visualized along the crystallographic b-axis using data from Frentzel-Beyme et al. [63] and Gao et al. [64]. Hydrogen atoms are omitted for clarity.

(II)-MXene film, a MXene film (90 nm thick) filtrated on a porous α-Al_2O_3 disk (70 nm pore size in the top layer, Fraunhofer IKTS) was immersed into 10 mL $Zn(NO_3)_2{\cdot}6H_2O$-DMF (*N,N*-dimethylformamide, 0.5 M) solution at 303 K for 24 h.

2.2. Preparation of ZIF-62 membranes

The solvothermal synthesis of ZIF-62 was based on the previously reported recipe [65], with additional use of sodium formate for membrane preparation. In a beaker, 10 mL DMF was added followed by dissolving 0.0222 g benzimidazole and 0.1148 g imidazole. The mixture was stirred for 5 min before adding 0.1116 g $Zn(NO_3)_2{\cdot}6H_2O$ and 1 mL $NaHCO_2$ (0.0128 g) methanolic solution. The aforementioned Al_2O_3 disk, which was modified with Zn (II)-MXene film, was placed vertically in a Teflon-lined stainless-steel autoclave. The loaded autoclave was placed in an oven at 373 K for 48 h followed by natural cooling to ambient temperature. The as-prepared polycrystalline membrane was washed with DMF once and activated by a series of methanol-DMF mixtures as reported by Dong et al. [26] To prepare a glass membrane, the melt-quenching process was employed. Specifically, the process involved heating the aforementioned polycrystalline membrane under flowing Ar to 723 K with a heating rate of 10 K min^{-1} for 10 min to form the melt, followed by naturally cooling back to room temperature by switching off the heating element of the tube oven (Carbolite MTF 12/50/250).

2.3. Characterization

To determine the melting temperature (T_m) and the glass transition temperatures (T_g) of ZIF-62, differential scanning calorimetry (DSC) measurements were performed on a Netzsch DSC 204 F1 Phoenix instrument under a constant nitrogen flow of 20 mL min^{-1}. Samples were heated to 768 K at 10 K min^{-1} and cooled to 298 K with the same rate. Analysis of thermal data was performed with the Netzsch Proteus software. T_m was determined as the peak offset, whereas T_g was defined as the peak onset. The crystalline structure of the samples was examined by X-ray diffraction patterns (XRD) recorded using a Bruker D8 Advance diffractometer with Cu–Kα radiation (40 kV and 40 mA). Data were collected over a range of 4°–40° with a step size of 0.04°. The chemical composition and bonding of the samples were analyzed by Fourier-transform infrared (FTIR) spectra acquired from 600 cm^{-1} – 4000 cm^{-1} using an Agilent Cary 630 spectrometer. Morphological features and elemental distributions of the prepared samples were captured using field-emission scanning electron microscopes (FE-SEM), specifically the JEOL JSM-6700F or the JSM-7610FPlus equipped with twin energy-dispersive X-ray spectrometers (EDXS, Bruker XFlash 6|60). The gas adsorption isotherms were measured on a Mircromeretics ASAP 2020 porosimetry system. ZIF-62 polycrystalline and glass powders were degassed under a dynamic vacuum at 473 K for 10 h prior to data collection. The adsorption behavior of was recorded at 293 K up to 120 kPa.

To probe the pore size of crystalline and glass samples, positron annihilation lifetime spectra were recorded using a conventional fast-fast coincidence lifetime spectrometer (Ortec, USA) with a time resolution of 241 ps and a channel width of 13 ps. In the measurements, a ^{22}Na positron source with an activity close to 20 μCi was encapsulated in Kapton films (Nilaco, Japan), and positioned between two identical disk samples, with each spectrum being recorded with over 1.5×10^6 counts. Using the PATFIT routine, the detailed positron lifetime parameters were analyzed from the spectra, with each spectrum undergoing a source correction by subtracting 402 ps and reducing by 9.981 % of the data. The third lifetime component τ_3, resulted from the *ortho*-positronium (*o*-Ps) annihilation process, was used to calculate the average radius of the free volume cavity R according to the Tao-Eldrup model [66,67]:

$$\tau_3 = 0.5\left[1 - \frac{R}{R+\Delta R} + \frac{1}{2\pi}\sin\left(\frac{2\pi R}{R+\Delta R}\right)\right]^{-1} \quad (1)$$

where ΔR is an empirical parameter (165.6 pm) derived from fitting the observed *o*-Ps lifetimes in molecular solids. The relative fractional free volume (*FFV*) was then obtained assuming spherical free volume using the following equation [68,69]:

$$FFV = C\frac{4}{3}\pi R^3 I_3 \quad (2)$$

where C is a constant with a value of 0.0018, and I_3 is the relative intensity of the third component τ_3.

2.4. Gas permeation measurements

Following the Wicke-Kallenbach method, permeation tests were conducted using a home-made gas-permeation apparatus as illustrated in Fig. S1. The prepared polycrystalline and glass membranes were mounted into a stainless-steel permeation cell and sealed with O-rings (Kalrez Spectrum™ 6375). Flow rates for both feed and sweep gases were controlled by mass flow controllers (Bronkhorst, EL-Flow®), with pressure monitored by digital pressure gauges on both sides. Temperature within the permeation cell was regulated by a setup that included a heating tape (Horst HBS) and a temperature regulator (Juchheim LTR 4200). Component concentrations in the permeate were determined by an Agilent 7890A on-line gas chromatograph.

During single-gas permeation, a flow rate of 25 mL min^{-1} was employed on the feed side, while for equimolar mixed-gas permeation a total flow rate of 50 mL min^{-1} (each gas at 25 mL min^{-1}) was applied. In the CO_2-stability test, 1 mL min^{-1} of CO_2 was added to the feed gas. For the hydrostability test, steam (3 vol%, 100% relative humidity) was introduced into the feed gas after passing through a water tank at 298 K. In all instances, 25 mL min^{-1} argon was applied on the sweep side. At least five measurements were conducted for one sample after the system reached a steady state. The permeance of component i (P_i) was determined using the equation:

$$P_i = \frac{N_i}{A(p_i - p_i')} \quad (3)$$

where N_i is the permeation rate of component i (mol s^{-1}), A corresponds to the membrane area (m^2), and p_i and p_i' denote the partial pressure of component i on the feed and permeate sides (Pa), respectively.

The selectivities (α for single-gas and $\alpha_{i/j}$ for mixed-gas permeation) were calculated as follows:

$$\alpha = \frac{P_i}{P_j} \quad (4)$$

$$\alpha_{i/j} = \frac{y_i/y_j}{x_i/x_j} \quad (5)$$

where x and y are the molar fractions of components i and j on the feed and permeate sides, respectively.

3. Results and discussion

3.1. Characterization of MXene and ZIF-62 powder

The MXene nanosheets ($Ti_3C_2T_x$) were prepared by selectively etching the Al element from the precursor Ti_3AlC_2 using HF solution in-situ generated through dissolving LiF in hydrochloric acid. This etching process resulted in the formation of abundant termination groups (T_x), such as –OH, =O, and –F, on the surface of the nanosheets, imparting the nanosheets with a negative ζ-potential. The SEM images in Figs. S2 and S3 demonstrate that most of MXene nanosheets are transparent to the

electron beam (as the anodic aluminum oxide object holder beneath the nanosheets remains clearly visible) despite variations in ultrasonication and centrifugation durations. A corresponding statistical analysis on the size of nanosheets is given in Fig. S4. It is evident that the nanosheets significantly reduce in size after centrifugation, whereas minimal variation is found among nanosheets produced with different ultrasonication durations. Indeed, ultrasonication serves to enhance the yield of single-layer/few-layer nanosheets, while centrifugation effectively removes multi-layer nanosheets/unetched precursor (see Fig. S3a). In this study, we opted for a 60-min duration for both ultrasonication and centrifugation, aiming to achieve a balance between experimental efficiency and MXene nanosheet yield. For details on the filtration of MXene thin films on α-Al_2O_3 supports (Note: not anodic aluminum oxide object holder) and the characterization on host of metal ions, please refer to our previous report [24].

After solvothermal synthesis, ZIF-62 polycrystalline membranes were formed on MXene-modified α-Al_2O_3 supports, with the ZIF-62 polycrystalline powder being collected from the same autoclave. To ascertain the suitability of this material for glass membrane preparation, differential scanning calorimetry analysis was firstly conducted on the ZIF-62 powder. As shown by the first upscan in Fig. 2, the polycrystalline powder releases solvent from 425 K to 645 K, then melts after 705 K. After quenching to room temperature, the second upscan indicates that the ZIF-62 glass has a glass transition temperature of 594 K. The measured values for T_m and T_g consistent well with the literature [70]. The thermal data confirm that our experimental treating temperature of 723 K is sufficiently high to transition a polycrystalline ZIF-62 membrane into a glass membrane.

3.2. Characterization of ZIF-62 membranes

We conducted comprehensive characterizations of both the ZIF-62 polycrystalline membranes and the glass membranes. The XRD patterns in Fig. 3a verify the purity of the polycrystalline powder and membrane, both showing ZIF-62 (CCDC code: 1849816) as the single phase. The absence of reflections from the MXene film was anticipated due to the growth of ZIF-62 within the film (see Figs. 5 and S12), leading to the disruption of the regular stacking of MXene nanosheets and consequently the disappear of 00*l* reflections [24,71,72]. Following the melt-quenching process, the crystalline reflections of the membrane disappear, indicating the long-range disorder of glass membrane. As

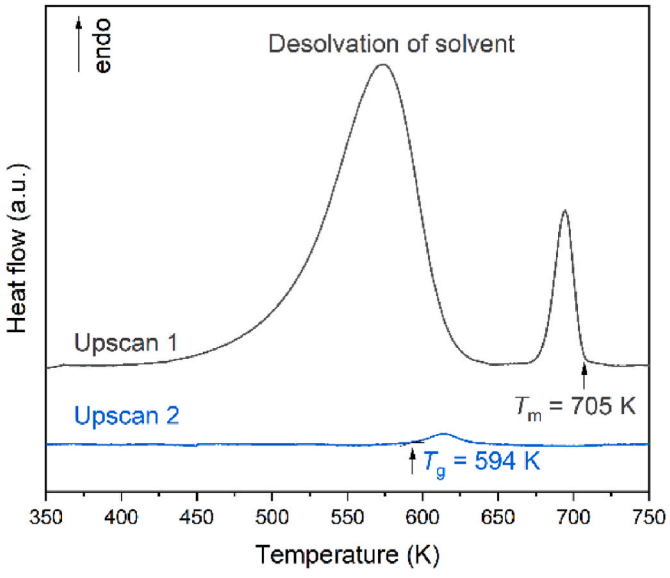

Fig. 2. First and second DSC upscans for ZIF-62 crystal and glass conducted under a nitrogen atmosphere.

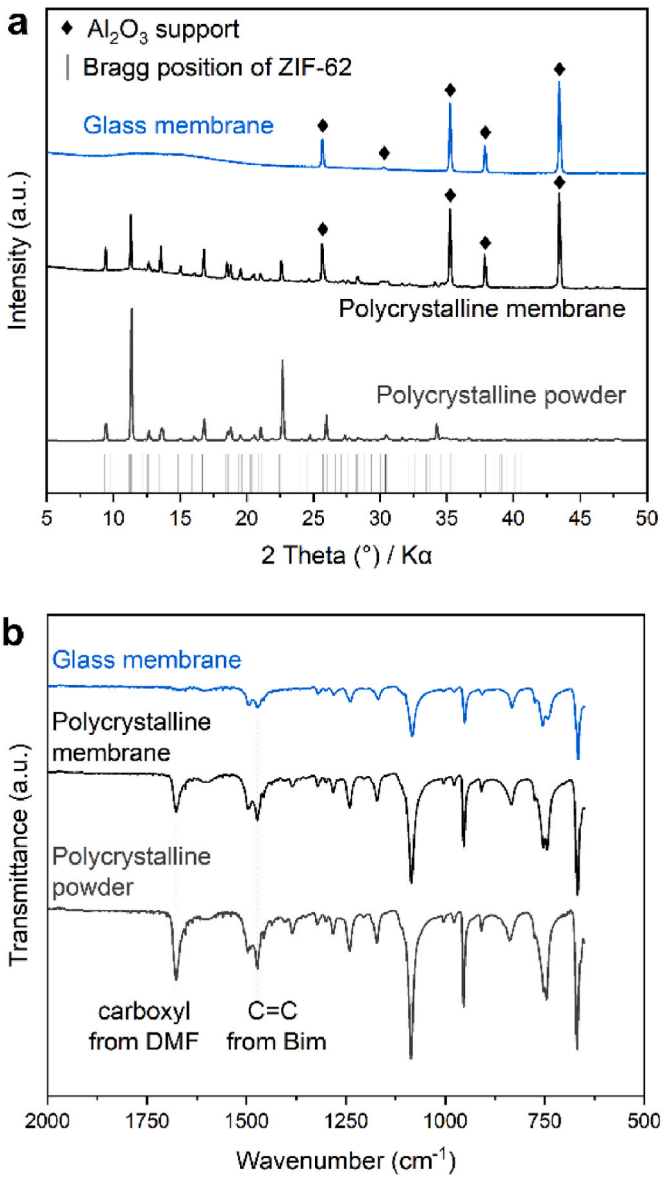

Fig. 3. (a) XRD patterns and (b) FTIR spectra of ZIF-62 polycrystalline powder, polycrystalline membrane, and glass membrane. Bragg positions of ZIF-62 are determined using the structure data (CCDC code: 1849816) from Frentzel-Beyme et al. [63].

elucidated by the FTIR spectra in Fig. 3b, the vibrational frequencies within the glass structure align with those of the polycrystalline membrane and powder, with the exception of a noticeable peak at around 1675 cm^{-1}, which is attributed to the carbonyl stretching vibration of the solvent DMF. This finding highlights the maintenance of structural integrity in the organic linkers throughout the melt-quenching process.

In terms of microporosity, a comparative CO_2 adsorption study between ZIF-62 polycrystal and glass indicates that the latter retained its microporous characteristics. As shown in Fig. S7, the adsorbed amount of CO_2 at 293 K and 1 bar declines from 1.38 mmol g^{-1} to 0.51 mmol g^{-1} after vitrification. To further assess the pore size alterations in ZIF-62 before and after vitrification, we employed positron annihilation spectroscopy measurements on its polycrystalline powder, glass powder, and glass membranes. Fig. 4 displays the diameter-intensity relationships along with comparison to literature values. Notably, some studies have performed four-component fitting instead of three-component fitting, yielding aperture diameters and cavity diameters around 3 Å and 6 Å, respectively [68,73]. As shown in Fig. 4b, ZIF-62 has a cag topology,

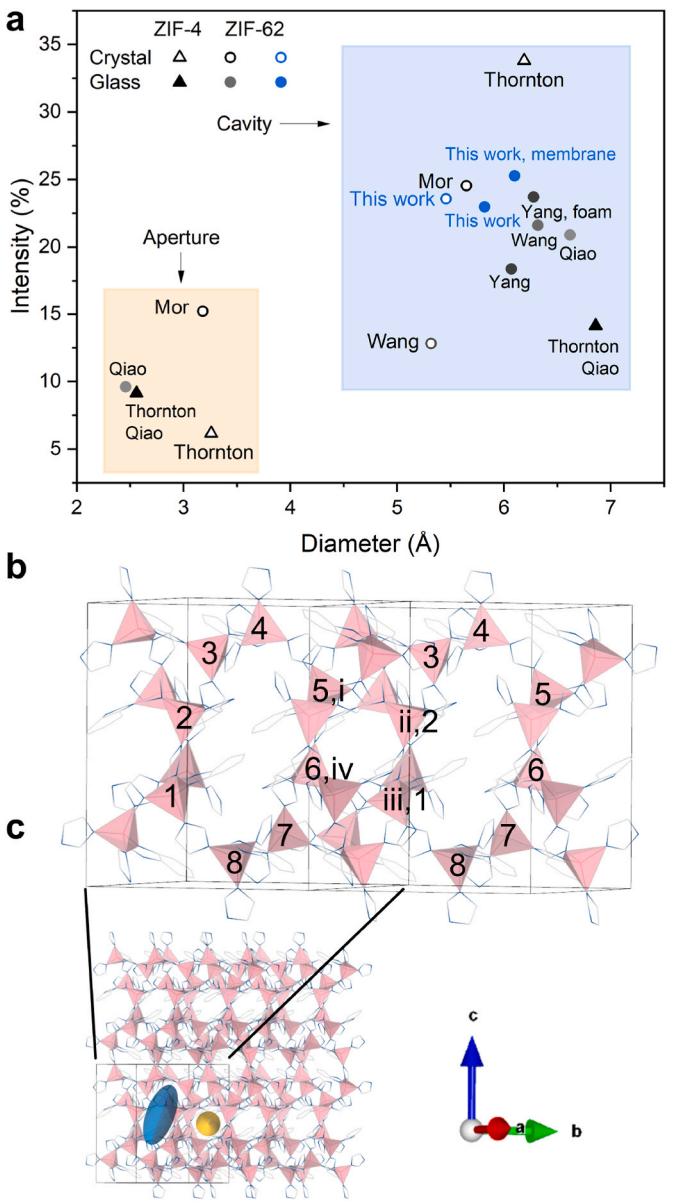

Fig. 4. (a) Cavity diameter of ZIF-62 polycrystalline powder, glass powder, and glass membranes calculated by fitting positron annihilation lifetime spectra. Data from literature are plotted in black and gray points [43,46,68,69,73]. More details can be found in Tables S2–S3. (b) Structure of ZIF-62 (1× 2× 1 cell, CCDC code: 1849816) showing the eight- and four-membered-rings. (c) Schematic illustration of a ZIF-62 2 × 2 × 2 cell with aperture and cavity shown in yellow and blue, respectively. Pink tetrahedral is ZnN_4. Hydrogen atoms are omitted for clarity. (For interpretation of the references to colour in this figure legend, the reader is referred to the Web version of this article.)

which is isotopological with the mineral variscite $CaGa_2O_4$ [74]. In its unit cell, the largest ring is an eight-membered ring. The tetrahedra numbered 5 and 6 form four-membered rings with the tetrahedra numbered ii and iii in the adjacent unit cells. These eight- and four-membered rings do not form a closed cage structure. Instead, the apertures and cavities shown in Fig. 4c are formed by multiple unit cells surrounded in three dimensions. This inherent ambiguity leads to a large difference between the calculated and measured values for aperture and cavity as summarized in Table S1. It is noteworthy that in the studies by Mor et al. [73] and Qiao et al. [68], deviations associated with the third lifetime component are more pronounced than those of the fourth (see Tables S2–S3). Nevertheless, results from Mor et al. [73] and Qiao et al. [68] collectively indicate that after the glass transition, the aperture diameter decreases while the cavity diameter increases. This trend is consistent with the findings from CO_2 adsorption calculations [40]. Similarly, Thornton et al. [69] observed consistent trend in their study on ZIF-4, which shares the cag topology with ZIF-62.

Our analyses favored a three-component fitting as it produced more coherent results compared to a four-component approach. The latter resulted in intensity discrepancies greater than the fitted intensity values. Fig. 4 showcases that the cavity diameter calculated from our fitted τ_3 values falls within the range reported in the literature. After the crystal-glass transition, the cavity diameter of ZIF-62 increases from 5.46 Å to 5.82 Å for glass powder and to 6.10 Å for glass membrane, consistent with literature reports (cf. Wang et al. [43], Mor et al. [73] and Qiao et al. [68]). Interestingly, the glass membranes exhibit a slightly larger cavity diameter than the glass powder, a trend also found in the work of Yang et al. [46] on glass foam. This hints that the sample preparation process can influence the measurement and fitting outcomes.

The morphological features and elemental distributions of ZIF-62 polycrystalline and glass membranes were then examined using SEM and EXDS. Similar to ZIF-67 [24], the crystalline grains of the ZIF-62 polycrystalline membrane interconnect closely with each other. In SEM images captured at various magnifications (Fig. S8), non-selective defects are seldom to be found. Besides, the elemental distributions in Figs. S10 and S11 display the coexistence of Zn and Ti at the lower portion of the polycrystalline membrane, precisely where the MXene film was anticipated to be located. This observation offers direct evidence supporting the preferential nucleation and growth of ZIF-62 on Zn (II)-MXene films. We note that the Zn signal is very weak in the alumina support.

Regarding the ZIF-62 glass membrane, Figs. 5 and S9 illustrate that the membrane surface becomes smooth and dense, and the boundaries between crystalline grains vanish after the melt-quenching process. Similar to the polycrystalline membrane, the glass membrane also exhibits regions where both Zn and Ti coexist, with no noticeable Zn signals within the support (Figs. S10 and S11). Changes in membrane thickness also serve as evidence that the majority of the glass melt did not penetrate into the support. While the polycrystalline membrane had an average thickness of 13.6 ± 2.3 μm, this value decreased to 10.7 ± 1.0 μm after its transformation into the glass membrane. This corresponds to a relative shrinkage of 21.3%, well consistent with the findings by Stepniewska et al. [75] obtained using a heating microscope. The penetration phenomenon differs from the work of Wang et al. [43], where the prepared glass melt penetrates heavily into supports. Two possible reasons can be considered. First, in this study, a MXene thin film was employed to modify the porous alumina support, and the stacked layers of MXene nanosheets acted as a barrier against the infiltration of the glass melt. Second, because of the preferential nucleation of ZIF-62 on the MXene film, the alumina support could be oriented vertically during the solvothermal reaction. In the work of Wang et al. [43], the support is positioned horizontally, leading to the ingress of more ZIF-62 particles into the porous support during the solvothermal growth process.

3.3. Gas separation performance of ZIF-62 membranes

Single-gas tests were conducted at 303 K and 1 bar for the ZIF-62 polycrystalline and glass membranes. The permeation results, illustrated in Fig. 6a, reveal that the ZIF-62 polycrystalline membranes predominantly favor the permeation of He. The observed selectivities slightly exceed the corresponding Knudsen selectivities. However, a marked contrast emerges when examining the ZIF-62 glass membranes. The selectivities for He/N_2, He/CH_4, and CO_2/N_2 increase when compared to their polycrystalline counterparts, recording values of 14.0, 10.6, and 29.9, respectively, as depicted in the inset of Fig. 6a. Alongside this, it was noted that the permeances for most gases sharply decreased

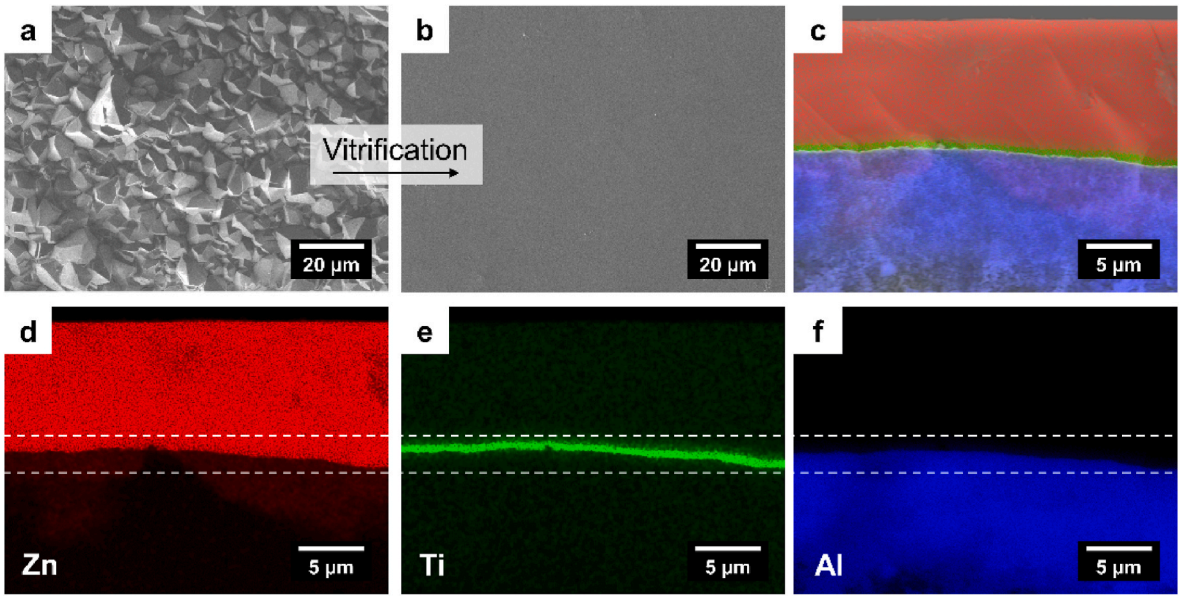

Fig. 5. SEM surface views of MXene assisted ZIF-62 (a) polycrystalline and (b) glass membranes. (c) SEM fractured cross-sectional view of the glass membrane. (d–f) EDXS elemental distributions corresponding to (c). Dashed lines indicate the region of the Ti signal, guiding the reader to observe the coexistence of Zn and Ti.

after vitrification. For instance, the N_2 permeance plummeted from 53.8 GPU in the polycrystalline membrane to a mere 1.5 GPU. Yet, intriguingly, the CO_2 permeance remained relatively stable, leading to an elevated CO_2/N_2 selectivity for the glass membrane. Equimolar mixed-gas tests for both the polycrystalline and glass membranes (Fig. 6b) demonstrate similar trends to single-gas tests, with a slight reduction in the permeance of He possibly due to gas competition during the mixed-gas tests [76–78].

The ZIF-62 crystal presents a complex pore structure: a possible aperture is formed by overlapping of multiple unit cells (Fig. 4b,c). Theoretical calculations predict its crystallographic aperture diameter is smaller than 0.26 nm [79–81]. A subsequent study discerns an aperture diameter of approximately 0.43 nm by analyzing the adsorption behavior of different gases on ZIF-62 crystalline powder [80]. However, pressure changes are required to allow adsorbates to access the micropores of ZIF-62 during a gas adsorption measurement (cf. Fig. S7). Such pressure adjustments can lead to structural alterations in the ZIF pores, a phenomenon known as gate-opening [82,83]. From the single-gas permeation test outcomes, the pore size cut-off for the ZIF-62 polycrystalline membranes is estimated to lie between the kinetic diameter of He and CO_2, i.e. 0.26 nm and 0.33 nm.

For the glass membranes, the passageway originating from the crystalline ZIF-62 should be preserved at least in the short-range, since the distance of neighboring atoms (e.g. Zn–Zn) does not change up to 0.6 nm as observed by X-ray total scattering [68]. The enhanced He selectivity over other gases and the reduced permeance of He, N_2, and CH_4 might originate from the elimination of non-selective defects at grain boundary (Fig. 5) and the alteration of pore size as discussed above (Fig. 4), both resulting from the melting-quenching process. The transport of CO_2, in contrast to other gases, does not show a significant reduction due to the influence of the adsorption process. It is reported that ZIF-62 glass exhibits a higher isosteric heat of adsorption for CO_2 compared with its polycrystalline counterpart [43]. Fig. S7b shows that ZIF-62 glass has a higher CO_2/N_2 adsorption selectivity when compared with ZIF-62 polycrystals. An effect of higher affinity of ZIF-62 glass to CO_2 can also be found when comparing the CO_2/N_2 selectivity measured in the single-gas (Fig. 6a) and equimolar mixed-gas tests (Fig. 6b), where the glass membranes show higher selectivity due to the competitive adsorption of CO_2. In addition, Fig. S15 also indicates that increasing the feed pressure or raising the temperature results in a decrease in CO_2 permeance, proving that the transport of CO_2 in the glass membranes is controlled by the adsorption process.

Gas separation from 303 K to 423 K was then conducted to assess the thermal stability of the ZIF-62 glass membrane. The permeance of all gases, except for CO_2, increased with rising temperature as shown in Figs. 6c, S13 and S14. The selectivity of He/N_2 decreased marginally from 17.5 (303 K) to 17.4 (423 K), while the selectivity of He/CH_4 showed a slight increase from 12.1 (303 K) to 13.9 (423 K). The He/N_2 selectivity is higher than the He/CH_4 selectivity, since ZIF-62 glass shows preferential adsorption of CH_4 over N_2 [43,46,55]. Activation energies for different gases were determined based on the permeance data at various temperatures, and they were found to be closely similar except for CO_2 (Figs. S13–S15). This experimental evidence demonstrates that the membrane's structural integrity remained intact throughout the heating process from 303 K to 423 K, indicating its good thermal stability.

The effect of feed pressure on the separation performance of ZIF-62 glass membranes was then investigated. When the feed pressure was raised to 1.5 bar, the permeance of both He and N_2 remained virtually unchanged (Fig. 6d). As it slowly increased to 3 bar, the He permeance stayed consistent while the permeance N_2 gradually increased, leading to a drop in selectivity to 8.5. The selectivity returned to its initial value upon reducing the feed pressure back to 1.1 bar, implying that the glass membrane has negligible macroscopic defects. The separation properties for He/CH_4 under changing pressure (Fig. S14) resembled those of He/N_2. However, due to the increased role of adsorption-control in CH_4 transport, the selectivity for He/CH_4 began to decline at a lower pressure compared to He/N_2. As for CO_2/N_2 separation (Fig. S15), the CO_2 permeance decreased with increasing pressure. This decrease can be attributed to the fact that the driving force, described as the ratio between the amount of adsorbed CO_2 and its partial pressure, also diminished with the escalation of feed pressure [84].

In light of practical applications, preliminary tests assessing the chemical stability of ZIF-62 glass membranes were carried out. Raw natural gas contains trace acid gases, notably CO_2 and water [8,11]. To mimic these conditions, we exposed the glass membranes to a feed gas containing either 2 vol% CO_2 or 3 vol% water vapor. During the initial 48 h, as illustrated in Fig. 6e, a stable separation performance was observed. Upon introducing CO_2 after this period, the permeance and separation factor did not decline in the following 73 h. Under conditions

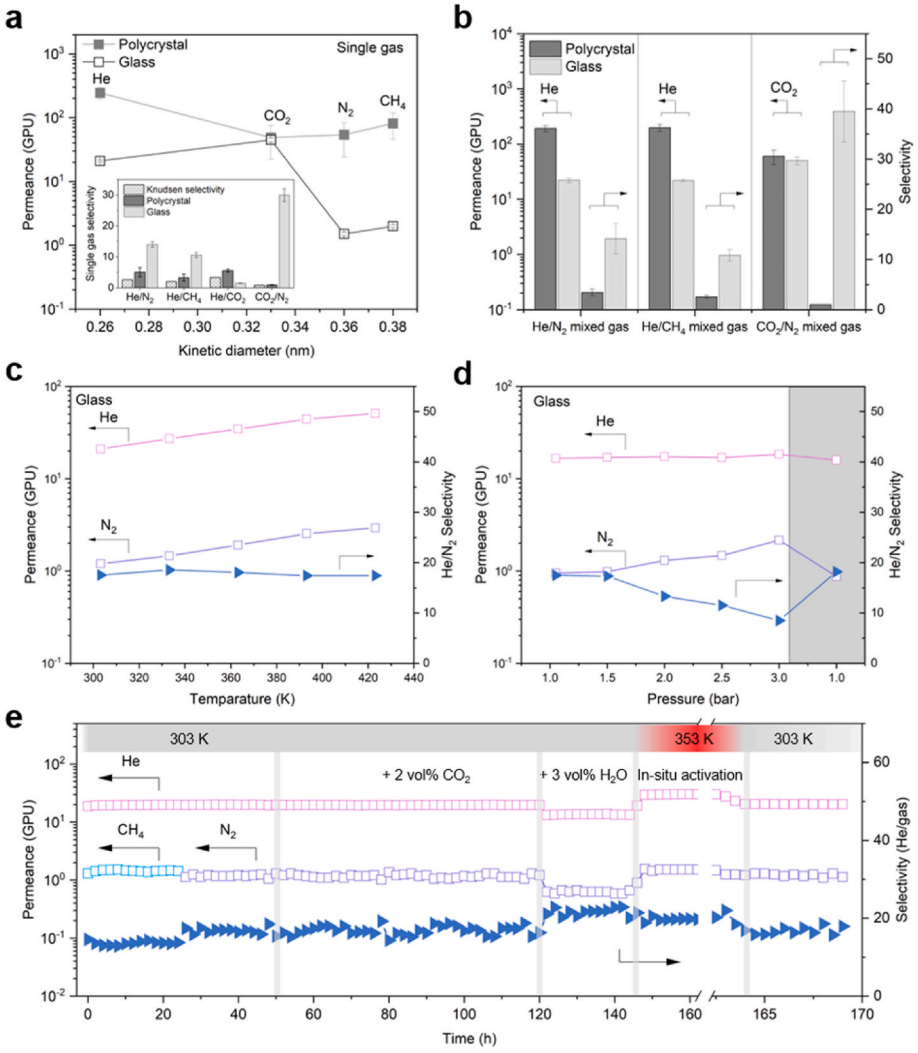

Fig. 6. Gas separation performance of ZIF-62 membranes. (a) Single-gas permeances measured at 303 K and 1 bar as a function of kinetic diameters. (b) Equimolar mixed-gas separation tests at 303 K and 1 bar for He/N_2 and He/CH_4. (c,d) Equimolar separation tests for He/N_2 as functions of (c) temperature and (d) feed-gas pressure. (e) Long-term separation of He/CH_4 and He/N_2 in presence of 2 vol% CO_2 or 3 vol% H_2O at 303 K and 1 bar. Error bars indicate the standard deviation of permeances and selectivities from three samples.

of 3 vol% water vapor (100% relative humidity), a minor decrease in the permeances of both He and N_2 was observed, attributed to the competitive transport of H_2O. This effect was reversible, with permeances recovering after in-situ activation at 353 K. This observation may be attributed to the unique adsorption behavior of non-polar CO_2 compared to polar H_2O within the glass membrane. H_2O molecules are known to be preferentially adsorbed by metal clusters in MOFs [85], leading to multilayers in micropores and subsequent reduction in pore size. In contrast, CO_2 may favor adsorption onto the ligands of ZIF-62 glass. An evidence is that fluorination of the benzimidazole ligand can enhance the CO_2 adsorption capacity by 19.5% compared with pristine ZIF-62 glass [55]. At a 2 vol% CO_2 concentration, pore blockage by CO_2 may not be evident due to ligand rotation. Overall, the membranes sustained stable separation performance for nearly 170 h, highlighting the remarkable chemical robustness of ZIF-62 glass membranes against CO_2 and H_2O exposures.

Fig. 7 provides a direct comparison of the separation performance of the glass membranes to other MOF membranes, illustrating the selectivity of He against N_2 and CH_4 as functions of He permeance [24, 86–96]. Most MOF membranes, including the ZIF-62 polycrystalline membranes, display selectivities of less than 5. In stark contrast, the ZIF-62 glass membranes achieve selectivities as high as 17.4 and 13.9 for He/N_2 and He/CH_4, respectively. We note in Fig. 7 that the selectivity of ZIF-8 membranes can be improved by incorporating C_{70} into ZIF-8 via a current-driven synthesis [96]. However, the selectivity remains lower than that of the ZIF-8 single crystal [25], probably due to the presence of the non-selective grain boundary.

4. Conclusions

Utilizing Zn (II)-MXene films as aids, we successfully fabricated ZIF-62 polycrystalline and glass membranes with thicknesses of 13.6 μm and 10.7 μm, respectively. The Zn (II)-MXene films ensured well-intergrown polycrystals within the membranes during the solvothermal synthesis on vertically placed supports. Only a minority (if any) of the glass melt was infiltrated into the supports during the vitrification process. The transformation to glass membranes led to the elimination of non-selective grain boundary defects, leading to a notable improvement in helium selectivity compared to the polycrystalline counterpart. Within a temperature range from 303 K to 423 K and pressures from 1 bar to 3 bar, the ZIF-62 glass membranes exhibited excellent performance of helium separation from N_2 and CH_4. The membranes demonstrated a helium permeance of approximately 51 GPU and selectivities of 17.4 and 13.9 for N_2 and CH_4 at 423 K, respectively, surpassing current MOF

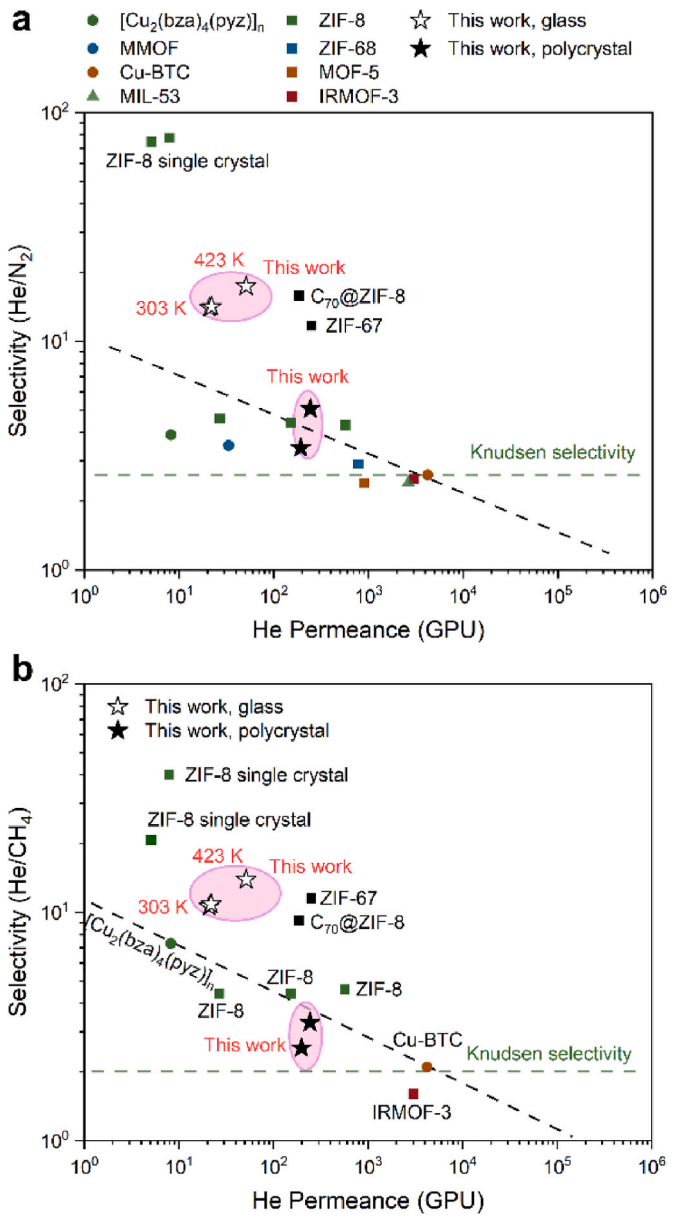

Fig. 7. (a) Selectivities of He/N_2 and (b) He/CH_4 plotted against He permeance, with comparisons to other MOF membranes reported in the literature [24,86–96]. The black dashed lines draw the upper limit of the current MOF membranes for He/N_2 and He/CH_4 separation and the green lines mark the corresponding Knudsen selectivities. Table S4 provides details on the data points. (For interpretation of the references to colour in this figure legend, the reader is referred to the Web version of this article.)

membranes. Long-term stability tests revealed that the glass membrane's separation efficiency for He/N_2 and He/CH_4 mixtures can operate stably for at least 170 h, even in the presence of 2 vol% CO_2 and 3 vol% H_2O.

CRediT authorship contribution statement

Zhijun Zhao: Writing – review & editing, Writing – original draft, Visualization, Validation, Methodology, Investigation, Formal analysis, Data curation, Conceptualization. **Li Ding:** Writing – review & editing, Validation, Investigation, Formal analysis, Data curation. **Alexander Mundstock:** Writing – review & editing, Visualization, Methodology, Investigation. **Oliver Stölting:** Formal analysis, Investigation, Writing – review & editing, Visualization. **Sebastian Polarz:** Writing – review & editing, Supervision. **Haihui Wang:** Supervision, Writing – review & editing. **Armin Feldhoff:** Writing – review & editing, Supervision, Project administration, Funding acquisition.

Declaration of competing interest

The authors declare that they have no known competing financial interests or personal relationships that could have appeared to influence the work reported in this paper.

Data availability

Data will be made available on request.

Acknowledgments

This work was financially supported by the Deutsche Forschungsgemeinschaft (DFG, German Research Foundation, project number 409987259). The authors thank L. Wagner and Prof. U. Giese for the DSC measurements, Dr. R. Almeev for access to the JSM-7610FPlus scanning electron microscope, and F. Steinbach for the technical assistance during energy-dispersive X-ray experiments.

Appendix A. Supplementary data

Supplementary data to this article can be found online at https://doi.org/10.1016/j.memsci.2024.122677.

References

[1] R. Clarke, W. Nuttall, B. Glowacki, Endangered helium: bursting the myth, Chem. Eng. 870 (2013) 32–36.
[2] P. Häussinger, R. Glatthaar, W. Rhode, H. Kick, C. Benkmann, J. Weber, H.-J. Wunschel, V. Stenke, E. Leicht, H. Stenger, Noble gases, in: G. Walter (Ed.), Ullmann's Encyclopedia of Industrial Chemistry, John Wiley & Sons, Ltd, 2001, pp. 392–448, https://doi.org/10.1002/14356007.a17_485.
[3] M. Alders, D. Winterhalder, M. Wessling, Helium recovery using membrane processes, Sep. Purif. Technol. 189 (2017) 433–440, https://doi.org/10.1016/j.seppur.2017.07.084.
[4] T.E. Rufford, K.I. Chan, S.H. Huang, E.F. May, A review of conventional and emerging process technologies for the recovery of helium from natural gas, Adsorpt. Sci. Technol. 32 (2014) 49–72, https://doi.org/10.1260/0263-6174.32.1.49.
[5] D.L. Gin, R.D. Noble, Designing the next generation of chemical separation membranes, Science 332 (2011) 674–676, https://doi.org/10.1126/science.1203771.
[6] D.S. Sholl, R.P. Lively, Seven chemical separations to change the world, Nature 532 (2016) 435–437, https://doi.org/10.1038/532435a.
[7] H.B. Park, J. Kamcev, L.M. Robeson, M. Elimelech, B.D. Freeman, Maximizing the right stuff: the trade-off between membrane permeability and selectivity, Science 356 (2017) eaab0530, https://doi.org/10.1126/science.aab0530.
[8] J. Sunarso, S.S. Hashim, Y.S. Lin, S.M. Liu, Membranes for helium recovery: an overview on the context, materials and future directions, Sep. Purif. Technol. 176 (2017) 335–383, https://doi.org/10.1016/j.seppur.2016.12.020.
[9] J. Balster, G. Baumgarten, D. Bergmair, Edle Gase trennen, Elements 59 (2017) 13–15.
[10] L. Xing, J. Qin, J. Wang, K. Wang, H. Wang, Z. Yang, G. He, X. Ruan, Polyimide membrane materials with multiple trifluoromethyl groups for helium enrichment from natural gases, Ind. Eng. Chem. Res. 62 (2023) 16081–16092, https://doi.org/10.1021/acs.iecr.3c02209.
[11] Z. Dai, J. Deng, X. He, C.A. Scholes, X. Jiang, B. Wang, H. Guo, Y. Ma, L. Deng, Helium separation using membrane technology: recent advances and perspectives, Sep. Purif. Technol. 274 (2021) 119044, https://doi.org/10.1016/j.seppur.2021.119044.
[12] H. Molavi, A. Shojaei, S.A. Mousavi, Improving mixed-matrix membrane performance via PMMA grafting from functionalized NH_2–UiO-66, J. Mater. Chem. A 6 (2018) 2775–2791, https://doi.org/10.1039/c7ta10480d.
[13] A. Akbari, J. Karimi-Sabet, S.M. Ghoreishi, Matrimid® 5218 based mixed matrix membranes containing metal organic frameworks (MOFs) for helium separation, Chem. Eng. Process 148 (2020) 107804, https://doi.org/10.1016/j.cep.2020.107804.
[14] Z.-X. Low, P.M. Budd, N.B. McKeown, D.A. Patterson, Gas permeation properties, physical aging, and its mitigation in high free volume glassy polymers, Chem. Rev. 118 (2018) 5871–5911, https://doi.org/10.1021/acs.chemrev.7b00629.
[15] X. Ma, K. Li, Z. Zhu, H. Dong, J. Lv, Y. Wang, I. Pinnau, J. Li, B. Chen, Y. Han, High-performance polymer molecular sieve membranes prepared by direct fluorination

for efficient helium enrichment, J. Mater. Chem. A 9 (2021) 18313–18322, https://doi.org/10.1039/d1ta04099e.
[16] M. Noack, P. Kölsch, R. Schäfer, P. Toussaint, J. Caro, Molecular sieve membranes for industrial application: problems, progress, solutions, Chem. Eng. Technol. 25 (2002) 221–230, https://doi.org/10.1002/1521-4125(200203)25:3<221::aid-ceat221>3.0.co;2-w.
[17] J. Shen, G. Liu, Y. Han, W. Jin, Artificial channels for confined mass transport at the sub-nanometre scale, Nat. Rev. Mater. 6 (2021) 294–312, https://doi.org/10.1038/s41578-020-00268-7.
[18] Y. Jiao, Q. Wu, W. Xu, W. Lai, L. Xiao, X. Mei, H. Zhang, S. Luo, Coordination enhancement of hydrogen and helium recovery in polybenzimidazole-based carbon molecular sieve membranes, Sep. Purif. Technol. 315 (2023) 123691, https://doi.org/10.1016/j.seppur.2023.123691.
[19] L. Lei, F. Pan, A. Lindbrathen, X. Zhang, M. Hillestad, Y. Nie, L. Bai, X. He, M. D. Guiver, Carbon hollow fiber membranes for a molecular sieve with precise-cutoff ultramicropores for superior hydrogen separation, Nat. Commun. 12 (2021) 268, https://doi.org/10.1038/s41467-020-20628-9.
[20] E.P. Favvas, N.S. Heliopoulos, S.K. Papageorgiou, A.C. Mitropoulos, G. C. Kapantaidakis, N.K. Kanellopoulos, Helium and hydrogen selective carbon hollow fiber membranes: the effect of pyrolysis isothermal time, Sep. Purif. Technol. 142 (2015) 176–181, https://doi.org/10.1016/j.seppur.2014.12.048.
[21] O. Sanyal, C. Zhang, G.B. Wenz, S. Fu, N. Bhuwania, L. Xu, M. Rungta, W.J. Koros, Next generation membranes — using tailored carbon, Carbon 127 (2018) 688–698, https://doi.org/10.1016/j.carbon.2017.11.031.
[22] C. Zhang, W.J. Koros, Ultraselective carbon molecular sieve membranes with tailored synergistic sorption selective properties, Adv. Mater. 29 (2017) 1701631, https://doi.org/10.1002/adma.201701631.
[23] M.C. Duke, S.J. Pas, A.J. Hill, Y.S. Lin, J.C.D. da Costa, Exposing the molecular sieving architecture of amorphous silica using positron annihilation spectroscopy, Adv. Funct. Mater. 18 (2008) 3818–3826, https://doi.org/10.1002/adfm.200800624.
[24] Z. Zhao, L. Ding, R. Hinterding, A. Mundstock, C. Belke, R.J. Haug, H. Wang, A. Feldhoff, MXene assisted preparation of well-intergrown ZIF-67 membrane for helium separation, J. Membr. Sci. 652 (2022) 120432, https://doi.org/10.1016/j.memsci.2022.120432.
[25] C. Chen, A. Ozcan, A.O. Yazaydin, B.P. Ladewig, Gas permeation through single-crystal ZIF-8 membranes, J. Membr. Sci. 575 (2019) 209–216, https://doi.org/10.1016/j.memsci.2019.01.027.
[26] X. Dong, K. Huang, S. Liu, R. Ren, W. Jin, Y.S. Lin, Synthesis of zeolitic imidazolate framework-78 molecular-sieve membrane: defect formation and elimination, J. Mater. Chem. 22 (2012) 19222, https://doi.org/10.1039/c2jm34102f.
[27] Y. Zhu, J. Ciston, B. Zheng, X. Miao, C. Czarnik, Y. Pan, R. Sougrat, Z. Lai, C.-E. Hsiung, K. Yao, I. Pinnau, M. Pan, Y. Han, Unravelling surface and interfacial structures of a metal–organic framework by transmission electron microscopy, Nat. Mater. 16 (2017) 532–536, https://doi.org/10.1038/nmat4852.
[28] W. Li, Metal–organic framework membranes: production, modification, and applications, Prog. Mater. Sci. 100 (2019) 21–63, https://doi.org/10.1016/j.pmatsci.2018.09.003.
[29] T. Ji, L. Liu, Y. Sun, Y. Liu, G. Xu, J. Yan, G. He, Y. Liu, Sub-zero temperature synthesis of pressure-resistant ZIF-8 membrane with superior C_3H_6/C_3H_8 separation performance, ACS Mater. Lett. (2022) 1094–1100, https://doi.org/10.1021/acsmaterialslett.2c00119.
[30] Y. Pan, W. Liu, Y. Zhao, C. Wang, Z. Lai, Improved ZIF-8 membrane: effect of activation procedure and determination of diffusivities of light hydrocarbons, J. Membr. Sci. 493 (2015) 88–96, https://doi.org/10.1016/j.memsci.2015.06.019.
[31] L. Sheng, C. Wang, F. Yang, L. Xiang, X. Huang, J. Yu, L. Zhang, Y. Pan, Y. Li, Enhanced C_3H_6/C_3H_8 separation performance on MOF membranes through blocking defects and hindering framework flexibility by silicone rubber coating, Chem. Commun. 53 (2017) 7760–7763, https://doi.org/10.1039/c7cc03887a.
[32] S. Park, K.Y. Cho, H.-K. Jeong, Enhancing the propylene/propane separation performances of ZIF-8 membranes by post-synthetic surface polymerization, J. Mater. Chem. A 10 (2022) 1940–1947, https://doi.org/10.1039/d1ta08705c.
[33] W. Li, P. Su, Z. Li, Z. Xu, F. Wang, H. Ou, J. Zhang, G. Zhang, E. Zeng, Ultrathin metal–organic framework membrane production by gel–vapour deposition, Nat. Commun. 8 (2017) 406, https://doi.org/10.1038/s41467-017-00544-1.
[34] X. Ma, P. Kumar, N. Mittal, A. Khlyustova, P. Daoutidis, K.A. Mkhoyan, M. Tsapatsis, Zeolitic imidazolate framework membranes made by ligand-induced permselectivation, Science 361 (2018) 1008–1011, https://doi.org/10.1126/science.aat4123.
[35] K. Eum, M. Hayashi, M.D.D. Mello, F. Xue, H.T. Kwon, M. Tsapatsis, ZIF-8 membrane separation performance tuning by vapor phase ligand treatment, Angew. Chem. Int. Ed. 58 (2019) 16390–16394, https://doi.org/10.1002/anie.201909490.
[36] P. Su, H. Tang, M. Jia, Y. Lin, W. Li, Vapor linker exchange of partially amorphous metal–organic framework membranes for ultra-selective gas separation, AIChE J. 68 (2022) e17576, https://doi.org/10.1002/aic.17576.
[37] Q. Ma, H. Jin, Y. Li, Tuning the adsorption selectivity of ZIF-8 by amorphization, Chem. Eur J. 26 (2020) 13137–13141, https://doi.org/10.1002/chem.202001249.
[38] H.T. Kwon, J. Kim, M. Shon, K. Eum, Postsynthetic modification strategies to improve polycrystalline metal-organic framework membranes, Mater. Today Sustain. 21 (2023) 100296, https://doi.org/10.1016/j.mtsust.2022.100296.
[39] C. Zhou, L. Longley, A. Krajnc, G.J. Smales, A. Qiao, I. Erucar, C.M. Doherty, A. W. Thornton, A.J. Hill, C.W. Ashling, O.T. Qazvini, S.J. Lee, P.A. Chater, N. J. Terrill, A.J. Smith, Y. Yue, G. Mali, D.A. Keen, S.G. Telfer, T.D. Bennett, Metal-organic framework glasses with permanent accessible porosity, Nat. Commun. 9 (2018) 5042, https://doi.org/10.1038/s41467-018-07532-z.
[40] L. Frentzel-Beyme, M. Klo, P. Kolodzeiski, R. Pallach, S. Henke, Meltable mixed-linker zeolitic imidazolate frameworks and their microporous glasses: from melting point engineering to selective hydrocarbon sorption, J. Am. Chem. Soc. 141 (2019) 12362–12371, https://doi.org/10.1021/jacs.9b05558.
[41] W. Xu, N. Hanikel, K.A. Lomachenko, C. Atzori, A. Lund, H. Lyu, Z. Zhou, C. A. Angell, O.M. Yaghi, High-porosity metal-organic framework glasses, Angew. Chem. Int. Ed. 62 (2023) e202300003, https://doi.org/10.1002/anie.202300003.
[42] S. Li, R. Limbach, L. Longley, A.A. Shirzadi, J.C. Walmsley, D.N. Johnstone, P. A. Midgley, L. Wondraczek, T.D. Bennett, Mechanical properties and processing techniques of bulk metal–organic framework glasses, J. Am. Chem. Soc. 141 (2018) 1027–1034, https://doi.org/10.1021/jacs.8b11357.
[43] Y. Wang, H. Jin, Q. Ma, K. Mo, H. Mao, A. Feldhoff, X. Cao, Y. Li, F. Pan, Z. Jiang, A MOF glass membrane for gas separation, Angew. Chem. Int. Ed. 59 (2020) 4365–4369, https://doi.org/10.1002/anie.201915807.
[44] Y. Zhang, Y. Wang, H. Xia, P. Gao, Y. Cao, H. Jin, Y. Li, A hybrid ZIF-8/ZIF-62 glass membrane for gas separation, Chem. Commun. 58 (2022) 9548–9551, https://doi.org/10.1039/d2cc03179e.
[45] H. Xia, H. Jin, Y. Zhang, H. Song, J. Hu, Y. Huang, Y. Li, A long-lasting TIF-4 MOF glass membrane for selective CO_2 separation, J. Membr. Sci. 655 (2022) 120611, https://doi.org/10.1016/j.memsci.2022.120611.
[46] Z. Yang, Y. Belmabkhout, L.N. McHugh, D. Ao, Y. Sun, S. Li, Z. Qiao, T.D. Bennett, M.D. Guiver, C. Zhong, ZIF-62 glass foam self-supported membranes to address CH_4/N_2 separations, Nat. Mater. 22 (2023) 888–894, https://doi.org/10.1038/s41563-023-01545-w.
[47] D. Ao, Z. Yang, Z. Qiao, Y. Sun, Z. Zhang, M.D. Guiver, C. Zhong, Metal–organic framework crystal–glass composite membranes with preferential permeation of ethane, Angew. Chem. Int. Ed. 62 (2023) e202304535, https://doi.org/10.1002/anie.202304535.
[48] O. Smirnova, S. Hwang, R. Sajzew, L. Ge, A. Reupert, V. Nozari, S. Savani, C. Chmelik, M.R. Reithofer, L. Wondraczek, J. Kärger, A. Knebel, Precise control over gas-transporting channels in zeolitic imidazolate framework glasses, Nat. Mater. 23 (2023) 262–270, https://doi.org/10.1038/s41563-023-01738-3.
[49] N. Ma, S. Horike, Metal–organic network-forming glasses, Chem. Rev. 122 (2022) 4163–4203, https://doi.org/10.1021/acs.chemrev.1c00826.
[50] A. Knebel, J. Caro, Metal–organic frameworks and covalent organic frameworks as disruptive membrane materials for energy-efficient gas separation, Nat. Nanotechnol. 17 (2022) 911–923, https://doi.org/10.1038/s41565-022-01168-3.
[51] R. Lin, M. Chai, Y. Zhou, V. Chen, T.D. Bennett, J. Hou, Metal–organic framework glass composites, Chem. Soc. Rev. 52 (2023) 4149–4172, https://doi.org/10.1039/d2cs00315e.
[52] J. Li, J. Wang, Q. Li, M. Zhang, J. Li, C. Sun, S. Yuan, X. Feng, B. Wang, Coordination polymer glasses with lava and healing ability for high-performance gas sieving, Angew. Chem. Int. Ed. 60 (2021) 21304–21309, https://doi.org/10.1002/anie.202102047.
[53] T.D. Bennett, A.L. Goodwin, M.T. Dove, D.A. Keen, M.G. Tucker, E.R. Barney, A. K. Soper, E.G. Bithell, J.-C. Tan, A.K. Cheetham, Structure and properties of an amorphous metal-organic framework, Phys. Rev. Lett. 104 (2010) 115503, https://doi.org/10.1103/PhysRevLett.104.115503.
[54] T.D. Bennett, D.A. Keen, J.-C. Tan, E.R. Barney, A.L. Goodwin, A.K. Cheetham, Thermal amorphization of zeolitic imidazolate frameworks, Angew. Chem. Int. Ed. 50 (2011) 3067–3071, https://doi.org/10.1002/anie.201007303.
[55] C. Ma, N. Li, D. Li, Z. Gu, Z. Qiao, C. Zhong, A self-supported aZIF-UC-4 glass membrane for gas separation, J. Membr. Sci. 683 (2023) 121873, https://doi.org/10.1016/j.memsci.2023.121873.
[56] X. Li, R. Lin, J. Hou, L. Wang, Sintering of metal-organic frameworks, Cell Rep. Phys. Sci. 3 (2022) 100932, https://doi.org/10.1016/j.xcrp.2022.100932.
[57] A. VahidMohammadi, J. Rosen, Y. Gogotsi, The world of two-dimensional carbides and nitrides (MXenes), Science 372 (2021) eabf1581, https://doi.org/10.1126/science.abf1581.
[58] L. Ding, Y. Wei, L. Li, T. Zhang, H. Wang, J. Xue, L.-X. Ding, S. Wang, J. Caro, Y. Gogotsi, MXene molecular sieving membranes for highly efficient gas separation, Nat. Commun. 9 (2018) 155, https://doi.org/10.1038/s41467-017-02529-6.
[59] J. Shen, G. Liu, Y. Ji, Q. Liu, L. Cheng, K. Guan, M. Zhang, G. Liu, J. Xiong, J. Yang, W. Jin, 2D MXene nanofilms with tunable gas transport channels, Adv. Funct. Mater. 28 (2018) 1801511, https://doi.org/10.1002/adfm.201801511.
[60] X. Hong, Z. Lu, Y. Zhao, L. Lyu, L. Ding, Y. Wei, H. Wang, Fast fabrication of freestanding MXene-ZIF-8 dual-layered membranes for H_2/CO_2 separation, J. Membr. Sci. 642 (2022) 119982, https://doi.org/10.1016/j.memsci.2021.119982.
[61] R. Li, X. Fu, G. Liu, J. Li, G. Zhou, G. Liu, W. Jin, Room-temperature in situ synthesis of MOF@MXene membrane for efficient hydrogen purification, J. Membr. Sci. 664 (2022) 121097, https://doi.org/10.1016/j.memsci.2022.121097.
[62] C. Liu, Y. Bai, W. Li, F. Yang, G. Zhang, H. Pang, In situ growth of three-dimensional MXene/metal–organic framework composites for high-performance supercapacitors, Angew. Chem. Int. Ed. 61 (2022) e202116282, https://doi.org/10.1002/anie.202116282.
[63] L. Frentzel-Beyme, M. Klo, R. Pallach, S. Salamon, H. Moldenhauer, J. Landers, H. Wende, J. Debus, S. Henke, Porous purple glass – a cobalt imidazolate glass with accessible porosity from a meltable cobalt imidazolate framework, J. Mater. Chem. A 7 (2019) 985–990, https://doi.org/10.1039/c8ta08016j.
[64] C. Gao, Z. Jiang, S. Qi, P. Wang, L.R. Jensen, M. Johansen, C.K. Christensen, Y. Zhang, D.B. Ravnsbk, Y. Yue, Metal-organic framework glass anode with an exceptional cycling-induced capacity enhancement for lithium-ion batteries, Adv. Mater. 34 (2022) 2110048, https://doi.org/10.1002/adma.202110048.

[65] M. Gustafsson, X. Zou, Crystal formation and size control of zeolitic imidazolate frameworks with mixed imidazolate linkers, J. Porous Mater. 20 (2012) 55–63, https://doi.org/10.1007/s10934-012-9574-1.
[66] S.J. Tao, Positronium annihilation in molecular substances, J. Chem. Phys. 56 (1972) 5499–5510, https://doi.org/10.1063/1.1677067.
[67] M. Eldrup, D. Lightbody, J.N. Sherwood, The temperature dependence of positron lifetimes in solid pivalic acid, Chem. Phys. 63 (1981) 51–58, https://doi.org/10.1016/0301-0104(81)80307-2.
[68] A. Qiao, T.D. Bennett, H. Tao, A. Krajnc, G. Mali, C.M. Doherty, A.W. Thornton, J. C. Mauro, G.N. Greaves, Y. Yue, A metal-organic framework with ultrahigh glass-forming ability, Sci. Adv. 4 (2018) eaao6827, https://doi.org/10.1126/sciadv.aao6827.
[69] A.W. Thornton, K.E. Jelfs, K. Konstas, C.M. Doherty, A.J. Hill, A.K. Cheetham, T. D. Bennett, Porosity in metal–organic framework glasses, Chem. Commun. 52 (2016) 3750–3753, https://doi.org/10.1039/c5cc10072k.
[70] R.S.K. Madsen, A. Qiao, J. Sen, I. Hung, K. Chen, Z. Gan, S. Sen, Y. Yue, Ultrahigh-field ^{67}Zn NMR reveals short-range disorder in zeolitic imidazolate framework glasses, Science 367 (2020) 1473–1476, https://doi.org/10.1126/science.aaz0251.
[71] M. Shekhirev, C.E. Shuck, A. Sarycheva, Y. Gogotsi, Characterization of MXenes at every step, from their precursors to single flakes and assembled films, Prog. Mater. Sci. 120 (2021) 100757, https://doi.org/10.1016/j.pmatsci.2020.100757.
[72] S. Uzun, S. Seyedin, A.L. Stoltzfus, A.S. Levitt, M. Alhabeb, M. Anayee, C.J. Strobel, J.M. Razal, G. Dion, Y. Gogotsi, Knittable and washable multifunctional MXene-coated cellulose yarns, Adv. Funct. Mater. 29 (2019) 1905015, https://doi.org/10.1002/adfm.201905015.
[73] J. Mor, P. Utpalla, J. Bahadur, D. Sen, S.K. Sharma, Porosimetry of zeolitic imidazolate frameworks using positron annihilation lifetime spectroscopy, Microporous Mesoporous Mater. 348 (2023) 112389, https://doi.org/10.1016/j.micromeso.2022.112389.
[74] R.N. Widmer, G.I. Lampronti, S. Anzellini, R. Gaillac, S. Farsang, C. Zhou, A. M. Belenguer, C.W. Wilson, H. Palmer, A.K. Kleppe, M.T. Wharmby, X. Yu, S. M. Cohen, S.G. Telfer, S.A.T. Redfern, F.X. Coudert, S.G. MacLeod, T.D. Bennett, Pressure promoted low-temperature melting of metal-organic frameworks, Nat. Mater. 18 (2019) 370–376, https://doi.org/10.1038/s41563-019-0317-4.
[75] M. Stepniewska, M.B. Stergaard, C. Zhou, Y. Yue, Towards large-size bulk ZIF-62 glasses via optimizing the melting conditions, J. Non-Cryst. Solids 530 (2020) 119806, https://doi.org/10.1016/j.jnoncrysol.2019.119806.
[76] Y. Liu, J. Liu, J. Hu, Noble gas separation by a MOF with one-dimensional channels, BMC Chem. Eng. 11 (2019) 1–7, https://doi.org/10.1186/s42480-019-0003-y.
[77] H. Guo, F. Shi, Z. Ma, X. Liu, Molecular simulation for adsorption and separation of CH_4/H_2 in zeolitic imidazolate frameworks, J. Phys. Chem. C 114 (2010) 12158–12165, https://doi.org/10.1021/jp908978q.
[78] A.V. Neimark, P.I. Ravikovitch, Calibration of pore volume in adsorption experiments and theoretical models, Langmuir 13 (1997) 5148–5160, https://doi.org/10.1021/la970266s.
[79] R. Banerjee, A. Phan, B. Wang, C. Knobler, H. Furukawa, M. Okeeffe, O.M. Yaghi, High-throughput synthesis of zeolitic imidazolate frameworks and application to CO_2 capture, Science 319 (2008) 939–943, https://doi.org/10.1126/science.1152516.
[80] J. Gandara-Loe, R. Bueno-Perez, A. Missyul, D. Fairen-Jimenez, J. Silvestre-Albero, Molecular sieving properties of nanoporous mixed-linker ZIF-62: associated structural changes upon gas adsorption application, ACS Appl. Nano Mater. 4 (2021) 3519–3528, https://doi.org/10.1021/acsanm.1c00010.
[81] Z. Zheng, Z. Rong, H.L. Nguyen, O.M. Yaghi, Structural chemistry of zeolitic imidazolate frameworks, Inorg. Chem. 62 (2023) 20861–20873, https://doi.org/10.1021/acs.inorgchem.3c02322.
[82] W. Morris, C.J. Doonan, H. Furukawa, R. Banerjee, O.M. Yaghi, Crystals as molecules: postsynthesis covalent functionalization of zeolitic imidazolate frameworks, J. Am. Chem. Soc. 130 (2008) 12626–12627, https://doi.org/10.1021/ja805222x.
[83] A. Knebel, B. Geppert, K. Volgmann, D.I. Kolokolov, A.G. Stepanov, J. Twiefel, P. Heitjans, D. Volkmer, J. Caro, Defibrillation of soft porous metal-organic frameworks with electric fields, Science 358 (2017) 347–351, https://doi.org/10.1126/science.aal2456.
[84] Y.S. Lin, I. Kumakiri, B.N. Nair, H. Alsyouri, Microporous inorganic membranes, Sep. Purif, Methods 31 (2002) 229–379, https://doi.org/10.1081/spm-120017009.
[85] J. Canivet, A. Fateeva, Y. Guo, B. Coasne, D. Farrusseng, Water adsorption in MOFs: fundamentals and applications, Chem. Soc. Rev. 43 (2014) 5594–5617, https://doi.org/10.1039/c4cs00078a.
[86] Y. Yoo, V. Varela-Guerrero, H.-K. Jeong, Isoreticular metal-organic frameworks and their membranes with enhanced crack resistance and moisture stability by surfactant-assisted drying, Langmuir 27 (2011) 2652–2657, https://doi.org/10.1021/la104775d.
[87] S. Takamizawa, Y. Takasaki, R. Miyake, Single-crystal membrane for anisotropic and efficient gas permeation, J. Am. Chem. Soc. 132 (2010) 2862–2863, https://doi.org/10.1021/ja910492d.
[88] F. Cao, C. Zhang, Y. Xiao, H. Huang, W. Zhang, D. Liu, C. Zhong, Q. Yang, Z. Yang, X. Lu, Helium recovery by a Cu-BTC metal-organic-framework membrane, Ind. Eng. Chem. Res. 51 (2012) 11274–11278, https://doi.org/10.1021/ie301445p.
[89] Z. Zhao, X. Ma, Z. Li, Y.S. Lin, Synthesis, characterization and gas transport properties of MOF-5 membranes, J. Membr. Sci. 382 (2011) 82–90, https://doi.org/10.1016/j.memsci.2011.07.048.
[90] R. Ranjan, M. Tsapatsis, Microporous metal organic framework membrane on porous support using the seeded growth method, Chem. Mater. 21 (2009) 4920–4924, https://doi.org/10.1021/cm902032y.
[91] N. Hara, M. Yoshimune, H. Negishi, K. Haraya, S. Hara, T. Yamaguchi, Diffusive separation of propylene/propane with ZIF-8 membranes, J. Membr. Sci. 450 (2014) 215–223, https://doi.org/10.1016/j.memsci.2013.09.012.
[92] O. Shekhah, R. Swaidan, Y. Belmabkhout, M. du Plessis, T. Jacobs, L.J. Barbour, I. Pinnau, M. Eddaoudi, The liquid phase epitaxy approach for the successful construction of ultra-thin and defect-free ZIF-8 membranes: pure and mixed gas transport study, Chem. Commun. 50 (2014) 2089–2892, https://doi.org/10.1039/c3cc47495j.
[93] D. Liu, X. Ma, H. Xi, Y.S. Lin, Gas transport properties and propylene/propane separation characteristics of ZIF-8 membranes, J. Membr. Sci. 451 (2014) 85–93, https://doi.org/10.1016/j.memsci.2013.09.029.
[94] A. Kasik, X. Dong, Y.S. Lin, Synthesis and stability of zeolitic imidazolate framework-68 membranes, Microporous Mesoporous Mater. 204 (2015) 99–105, https://doi.org/10.1016/j.micromeso.2014.10.050.
[95] Y. Zhang, Q. Gao, Z. Lin, T. Zhang, J. Xu, Y. Tan, W. Tian, L. Jiang, Constructing free standing metal organic framework MIL-53 membrane based on anodized aluminum oxide precursor, Sci. Rep. 4 (2014) 4947, https://doi.org/10.1038/srep04947.
[96] J. Han, H. Wu, H. Fan, L. Ding, G. Hai, J. Caro, H. Wang, Tuning the phase composition of metal–organic framework membranes for helium separation through incorporation of fullerenes, J. Am. Chem. Soc. 145 (2023) 14793–14801, https://doi.org/10.1021/jacs.3c03362.